Three-Dimensional Super Resolution Imaging using a Row-Column Array

Jensen, Jørgen Arendt; Ommen, Martin Lind; Øygard, Sigrid Husebø; Schou, Mikkel; Sams, Thomas; Stuart, Matthias Bo; Beers, Christopher; Thomsen, Erik Vilain; Larsen, Niels Bent; Tomov, Borislav Gueorguiev

Published in:
IEEE Transactions on Ultrasonics, Ferroelectrics and Frequency Control

Link to article, DOI:
10.1109/TUFFC.2019.2948563

Publication date:
2020

Document Version
Peer reviewed version

Three-Dimensional Super Resolution Imaging using a Row-Column Array

Jørgen Arendt Jensen[1], Martin Lind Ommen[1], Sigrid Husebø Øygard[1], Mikkel Schou[1], Thomas Sams[1], Matthias Bo Stuart[1], Christopher Beers[2], Erik Vilain Thomsen[1], Niels Bent Larsen[1] and Borislav Gueorguiev Tomov[1]

[1]Department of Health Technology,
Technical University of Denmark, DK-2800 Lyngby, Denmark
[2] BK Medical, 401 Science Park Road, State College, PA 16803, USA

***Abstract*—A 3-D super resolution (SR) pipeline based on data from a Row-Column (RC) array is presented. The 3 MHz RC array contains 62 rows and 62 columns with a half wavelength pitch. A Synthetic Aperture (SA) pulse inversion sequence with 32 positive and 32 negative row emissions are used for acquiring volumetric data using the SARUS research ultrasound scanner. Data received on the 62 columns are beamformed on a GPU for a maximum volume rate of 156 Hz, when the pulse repetition frequency is 10 kHz. Simulated and 3-D printed point and flow micro-phantoms are used for investigating the approach. The flow micro-phantom contains a 100 μm radius tube injected with the contrast agent SonoVue. The 3-D processing pipeline uses the volumetric envelope data to find the bubble's positions from their interpolated maximum signal and yields a high resolution in all three coordinates. For the point micro-phantom the standard deviation on the position is (20.7, 19.8 , 9.1) μm (x,y,z). The precision estimated for the flow phantom is below 23 μm in all three coordinates, making it possible to locate structures on the order of a capillary in all three dimensions. The RC imaging sequence's point spread function has a size of 0.58 $\times$ 1.05 $\times$ 0.31 mm^3 (1.17$\lambda\times$2.12$\lambda\times$0.63λ), so the possible volume resolution is 28,900 times smaller than for SA RC B-mode imaging.**

I. Introduction

Ultrasound super resolution imaging (SRI) was introduced by a number of groups for increasing the resolution of ultrasound imaging beyond the diffraction limit [1–6]. The approach is based on injection of a diluted ultrasound contrast agent to enable tracking of individual bubbles. The centroids of the bubble signals are calculated, and their tracks are determined and displayed to show an image of the vasculature. This can reveal the micro vasculature down to vessel sizes of 10 μm [7]. The images are acquired over several seconds to minutes generating Gbytes of data. Currently most SRI is conducted using 1-D array probes due to the large amount of data, and that few scanners are capable of full 3-D imaging. The 2-D SR images therefore have a high resolution in the imaging plane, but localization in the elevation direction is not possible. 2-D SRI therefore displays a summation of vessels in the elevation plane.

Visualization of 3-D SR volumes has been performed by several groups using mechanically translated linear array probes [6, 8, 9], but such a setup does not make it possible to estimate the out-of-plane location. SR has also been made using two orthogonal probes for 3-D localization in a line [10], and mechanical scanning is needed to cover a full volume. A matrix probe is, thus, needed for avoiding mechanical scanning.

Currently, the largest research scanners have 1024 channels [11, 12], and they generate around 20-50 Gbytes/s of data for 3 MHz probes, only making short acquisitions possible and precluding the use of high-frequency probes. They can handle 2-D arrays with $32 \times 32 = 1024 = N^2$ elements, which have been fabricated with $\lambda/2$ pitch (λ is the wavelength given by c/f_0, where c is the speed of sound and f_0 is transducer center frequency). This makes them suitable for phased array imaging, but severely limits their focusing ability due to their small size and hence high F-numbers (imaging depth divided by the probe width).

The problem can be somewhat alleviated by using sparse arrays, and Harput et al. [13] recently used a 512 elements sparse 2-D array based on a spiral pattern to acquire full 3-D SR imaging. Two 256 channels research scanners [14] were used for scanning of 200 μm cellulose tubes with a final localization precision of 18 μm. The main drawback of this approach is the many transducer channels needed to avoid grating lobes and the corresponding large amounts of data generated per second. Further, the probe is quite small ($\varnothing$ 10.4 mm), as it has to be nearly fully populated to avoid side and grating lobes, limiting the possible F-numbers.

An new approach is therefore needed for 3-D SR volumetric imaging. One possibility for reducing the number of elements by a factor of $N/2$ is the employment of Row-Column (RC) arrays as introduced by Morton and Lockwood [15], and later investigated by a number of groups [16–20]. Here, the array is addressed by either its rows or columns, and imaging can be conducted using synthetic aperture (SA) imaging schemes [21] for both a high resolution, deep penetration depth, and high volume rate. Furthermore, RC SA imaging schemes can have a low mechanical index due to the emission of cylindrical waves, making them ideally suited for contrast agent imaging. The RC arrays can be made large without having an excessive amount of elements, making it possible to both have low F-numbers for high resolutions and still have modest data rates from the arrays.

This paper presents a 3-D SR imaging method using a prototype 62 + 62 RC array [22] connected to the SARUS research scanner [11]. Two 3-D printed micro phantoms are used for validating the approach along with simulation of a point phantom. The precision of the pipeline is revealed from these simulations and measurements.

II. Methods

This Section describes the various methods used in the 3-D SR pipeline including the imaging scheme, processing pipeline, and statistical evaluation.

A. Imaging sequence and processing

The imaging sequence was optimized for a 62+62 RC PZT 3 MHz experimental probe with dimensions given in Table I. The probe includes a mechanical apodization at each end of the elements to reduce edge element artifacts as described in previous publications on the probe [19–22]. The volumetric RC SA imaging scheme consists of 32 virtual focus lines using 32 active elements per emissions. An F-number of -1 was used for emitting de-focused line sources with the focal point placed behind the probe surface and with a Hanning weighting to reduce side-lobes. The 32 different virtual lines were placed to generate a sliding aperture imaging sequence across the rows. Transmission were only made with the rows and reception was made with the column elements, resulting in 62 signals to be stored per emission. Pulse inversion imaging was conducted by emitting two 2 cycle sinusoidal 3 MHz waves, one positive and one negative, for each virtual line source. The imaging sequence was implemented on the the SARUS experimental scanner [11], with a transmit sampling frequency of 70 MHz. The receive sampling frequency was 23.7 MHz to preserve the second harmonic component in the signal.

TABLE I
RC 62 + 62 PZT probe dimensions.

Parameters	**62+62 RC**
Number of elements	62+62
Center frequency f_0	3 MHz
Wavelength λ	513 μm
Kerf	25 μm
Pitch	270 μm ($\approx \lambda/2$)
Apodization region length	4.05 mm
Element length	24.84 mm
Total Active Surface area	282.2 mm^2

Each emission was beamformed using a MATLAB based GPU beamformer [23] to generate a low resolution volume (LRV). The 32 different LRVs were summed to reveal a high resolution volume (HRV). A simplified schematic of the sequence can be seen in Fig. 1. The positive +LRV(1:32) and negative -LRV(1:32) beamformed emissions were summed to reveal a second harmonic HRV using pulse inversion. This data was then passed to the SRI processing pipeline described in Section II-B. The pulse repetition frequency (f_{prf}) was 10 kHz, and a pause of 10 ms was inserted between volumes to reduce the memory usage and extend the duration of the acquisition. The Mechanical Index (MI) of the sequence was determined to be 0.2 at 12 mm from the probe surface, which is the location of the micro-phantom flow channel. The actual MI in the phantom is probably slightly lower due to the attenuation in the phantom.

Three sets of measurements were performed using a precision translation stage. The RC probe was mounted on a Newport PG Series floating optical table (Irvine, California) for stability with the micro-phantoms mounted on a 8MR190-2-28 rotation stage combined with a 8MTF-75LS05 $x-y$ translation stage (Standa, Vilnius, Lithuania). These were used to align both micro-phantoms with the imaging axis, and to generate translation in the $x-y$ plane used for the validation described in Section III-B.

B. Processing pipeline

The processing pipeline consists of several stages. The first step is to beamform the stored RF data from the SARUS scanner using the beamforming strategy described by Rasmussen et al. [19, 21] implemented in Matlab and running on an Nvidia GeForce GTX 1050 Ti (Nvidia, Santa Clara, CA, USA) [23]. A volume with a size of $\pm 15\lambda$ in both the x and y directions are beamformed with a line density of $\lambda/2$ and covering the depth of the phantom. The sampling density in the z direction is

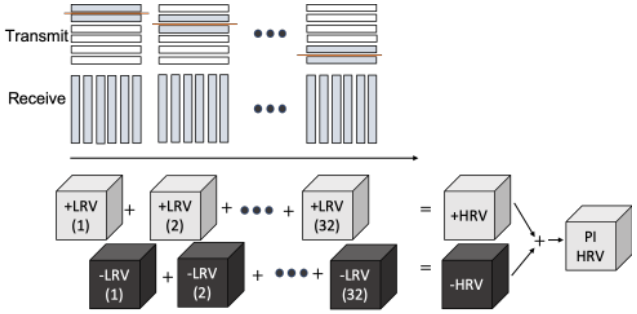

Fig. 1. The transmitting row elements and their translation across the aperture is shown in the top figure along with the receiving column elements. The time sequence of the positive and negative emissions and their combination is shown in the bottom figure.

$\lambda/16$. A matched filter is applied on the received signals. It is designed using the measured impulse response of the probe to match the first harmonic signal found in the linearly simulated data. The same filter is also used for PSF phantom. The positive and negative emissions are then subtracted to increase the signal-to-noise ratio (SNR). For the flow micro-phantom the second harmonic signal is employed, the filter is matched to this, and the two emissions are added. The full LRV is beamformed for all emissions with an F-number of 1.5 in transmit and 1 in receive with a dynamic Hanning apodization weighting the elements, and all emissions are added to generate the HRV. The mean value of the first 20 HRVs are averaged and subtracted from the processed HRVs to remove stationary objects in the processing. The envelope of the HRV is then found using a Hilbert transform and log compressed to a 40 dB dynamic range in relation to the data in the volume for finding locations.

The peak location can either be found from calculation of the centroid of a global maximum, or the peak location can be interpolated to increase the location accuracy. Experimentation with the data has shown that the interpolation scheme is the most stable and accurate method, and this is the one used in this paper.

The second stage finds bubble locations by interpolating the peak position by fitting a second order polynomial to the data and then finding its interpolated maximum position x_i, as:

$$x_i = i - \frac{0.5(d(i+1,j,k) - d(i-1,j,k))}{d(i+1,j,k) - 2d(i,j,k) + d(i-1,j,k)}, \qquad (1)$$

where i,j,k are the indices of the maximum and d is the envelope data for the volume. This is conducted in all three coordinates x_i, y_j, z_k with similar equations for an increased resolution in all three directions.

The third step used only on the point micro-phantom finds contiguous tracks of target locations. A target in a first HRV is used as a reference point, and the adjacent HRV is searched to find a detected target location lying within a radius of $r = v_s/f_r$ from the reference, where f_r is the volume rate and v_s is the maximum search velocity, where $v_s = 10$ mm/s was used. The track is terminated, if no target is found, and the whole track is discarded, if it does not contain more than 200 contiguous locations. No tracks were formed for the micro-flow phantom due to the high velocity employed, and all bubble locations in all images are shown in Section III-C.

C. Simulations and measurement phantoms

The method is evaluated using both simulations and measurements from two 3-D printed micro-phantoms, which are all described in this Section. The penetration depth is also determined from measurements on a tissue mimicking phantom with a 0.5 dB/[MHz cm] attenuation.

1) Simulation of 3-D SRI system: The SA RC sequence has been simulated using Field IIpro [24–26] to generate reference data, where the positions of the scatterers are known in the volume. The phantom contains a number of point targets located at a depth of 5, 15, and 25 mm at the center axis of the probe. It is used for determining the point spread function (PSF) of the imaging method.

2) Fabrication of micro-phantoms: Two micro-phantoms have been made and used for validating the approach. Both have been fabricated by 3-D printing of a PEGDA 700 g/mol hydrogel using stereo-lithography. The phantoms measure 21.1 $\times$ 8.16 $\times$ 11.9 mm^3, and the voxel size of the printer is $(\Delta x, \Delta y, \Delta z) = 10.8 \times 10.8 \times 20$ μm^3. More information about the fabrication process can be found in [27].

The first point phantom contains eight markers with a size of $10.8 \times 10.8 \times 20 = 233 \mu$m^3. The marker sizes are in all dimensions smaller than the imaging wavelength of 500 μm for the RC probe used, resulting in markers appearing as single targets in the B-mode volume. The markers are positioned with a minimum distance of 3 mm to ensure a clear separation of the reflected signals. The phantom is moved relative to the ultrasound probe using the $x-y$ translation stage in two experiments, one along x and one along y. An inter-volume movement of 12.5 μm is used to emulate a constant velocity of 1.95 mm/s at 156 Hz. After each movement the positions of the markers are determined and tracks for the targets are made.

The second flow micro-phantom contains a single cylindrical 100 μm radius channel placed 3 mm from the top surface of the phantom. After a 5.8 mm long

inlet, the channel bends 90° into a 7 mm long central region before bending 90° again into the 5.8 mm outlet. The flow channel was infused at 1.61 μL/s with SonoVue (Bracco, Milano, Italy) in a 1:10 dilution giving a peak velocity of 102.4 mm/s.

D. Statistical evaluation

The bubble locations are randomly distributed in the flow micro-phantom tube due to noise in the localization estimation, and some of them will appear to be located outside the phantom wall. The distribution of positions found can then yield an estimate of the localization precision. An estimate of the $y-z$ and $x-z$ precision can be obtained from the two straight segments of the 200 μm channel phantom. In the straight segments a line is fitted to the data and considered an estimate of the center of the channel, and the distance from each bubble to the center is calculated. Assuming the measurement uncertainty in each dimension is normal distributed, the radial distribution of all bubbles in the segment will follow the distribution

$$f(r) = 2\pi r \int_{|\vec{r}_t|<R} \frac{1}{\pi R^2} \frac{1}{2\pi\sigma^2} \exp\left(\frac{-|\vec{r}-\vec{r}_t|^2}{2\sigma^2}\right) d^2 r_t \quad (2)$$

where r is radial position, R is the radius of the tube, and σ is the standard deviation of the uncertainty. The integral is a convolution of a constant density $(1/(\pi R^2))$ with a two-dimensional Gaussian. The non-analytical integral (2) is estimated in a Monte-Carlo calculation and is a Rayleigh distribution convolved with a uniform disk distribution of radius $R = 100$ μm. The factor $2\pi r$ is the Jacobian needed to convert from Cartesian to cylindrical coordinates. The fraction of bubbles estimated to fall outside the tube can then be translated into an estimate for the standard deviation σ (localization precision), as is performed in Section III-C1

III. Result

A. Imaging performance

The performance of the imaging scheme has both been simulated and measured. The response from several point scatterers were simulated using Field II, and the FWHM was determined for the first harmonic signal to be (FWHM_x, FWHM_y, FWHM_z, $= 0.58 \times 1.05 \times 0.31$ mm $= (1.17\lambda \times 2.12\lambda \times 0.63\lambda)$ at a depth of 15 mm. The receive F-number is 1, so the PSF is close to the theoretical limit of λ. The transmit F-number is 1.5 and, thus, gives a slightly wider PSF in the y-direction along emissions.

The penetration depth of the scheme was determined using a uniformly scattering phantom model 571 (Danish Phantom Service, DK-3600 Frederikssund, Denmark) with a speed-of-sound of 1540 m/s and a uniform attenuation of 0.5 dB/[MHz cm]. Determining the SNR from ten independent measurements gave a penetration depth of 14 cm (SNR=0 dB).

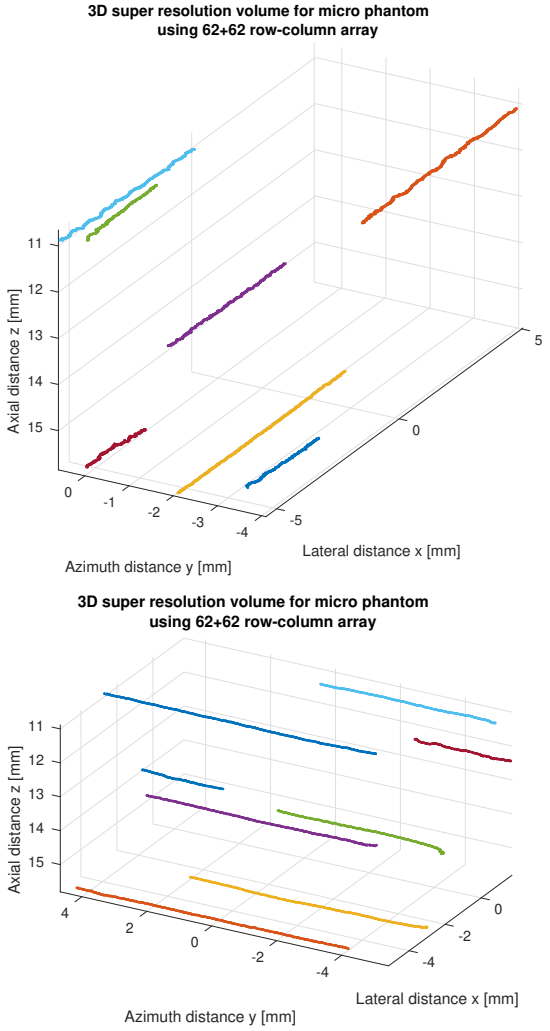

Fig. 2. Tracks estimated from mechanical translation of the PSF micro phantom where the colors indicate detected positions. The top graph is for translation in the x-direction and bottom for translation in y.

B. Validation in point micro-phantom

Fig. 2 shows the cumulative localized positions of 3-D printed markers within the micro phantom acquired over 640 beamformed volumes at the emulated speed of 1.95 mm/s. The top figure shows movement in the x-direction and in the y-direction at the bottom. Seven markers have been detected and are shown as colored points. The eighth marker was too weak to be detected. Lines are fitted to the positions using a least squares fit, as shown in Fig. 3 for one of the tracks. The deviations

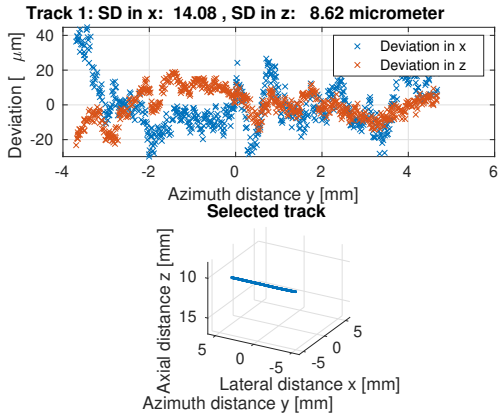

Fig. 3. Deviations calculated for one of the tracks, when a line has been fitted to the data. The bottom graph shows the estimated target locations, and the top graph shows the deviations in x and z, when the line has been subtracted from the target position.

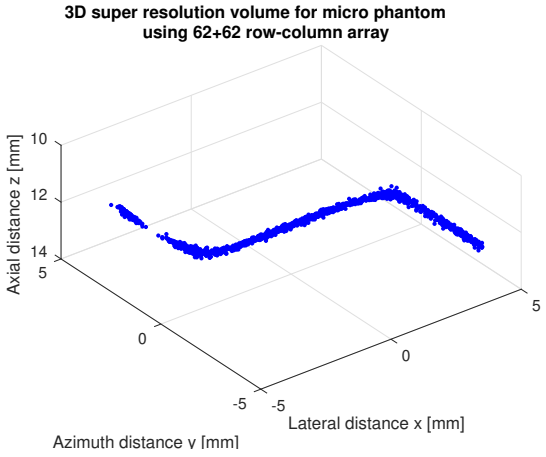

Fig. 4. View of the 200 μm channel phantom. Each blue dot represents a detected contrast agent bubble. See accompanying video for a 3-D view of the phantom.

from the fitted line are calculated and the standard deviations is estimated to $(\sigma_x, \sigma_y, \sigma_z) = (20.7, 19.8, 9.1)$ μm, when taking the average across all tracks.

C. 3-D SRI imaging

The measured data from the flow micro-phantom acquired from 400 frames of the SA imaging sequence has been processed by the SR pipeline, including beamforming and detection of bubble locations, using the interpolation scheme in (1). A 3-D view of the detected bubbles is shown in Fig. 4, where each blue dot is a detected bubble. The geometry of the phantom can clearly be seen.

1) Precision of bubble locations: Bubbles in the central part of the phantom (-2 mm $< x < 2$ mm) have been selected for estimating the localization precision in

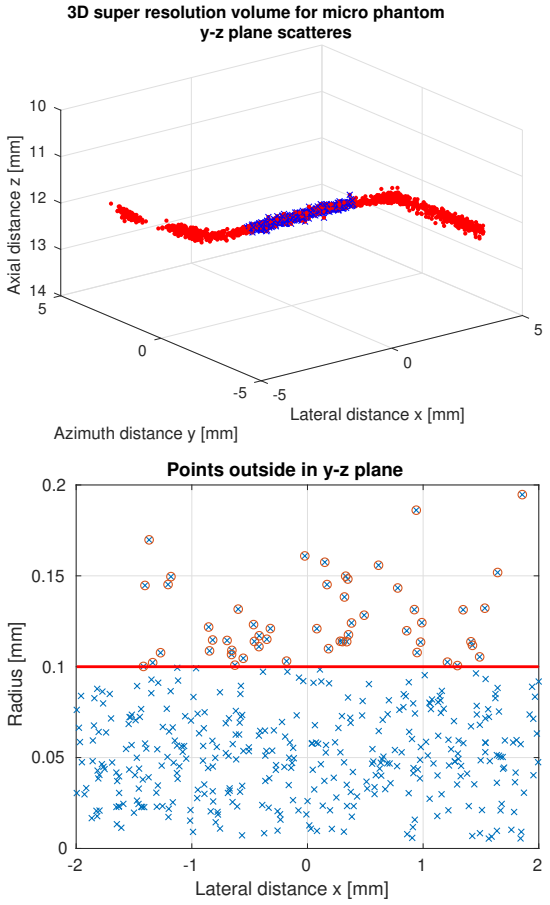

Fig. 5. Selected bubbles in the $y-z$ plane (blue crosses) for estimating precision (top graph), and the calculated radial position of the bubbles in the vessel (bottom graph). Blue crosses indicate bubbles inside the vessel and red circles indicates outside.

the $y-z$ plane as shown on the top in Fig. 5, where blue crosses indicate bubbles used for this estimation. Center lines for all selected bubbles are estimated with a least square fit as shown in Fig. 6. The channels center depth is at 12.0 mm from the probe, and the channel is slightly rotated in the $x-y$ plane (57 μm tilt of $x-y$ line in the top graph). These lines are used for calculating the radial positions of the bubbles in the vessel, as shown on the bottom figure in Fig. 5. Here, a blue cross indicates bubbles inside the vessel, and a red circle indicates bubbles outside of the vessel boundary, shown as the solid red line ($r = 100\,\mu$m). The same graph for the $x-z$ plane is shown in Fig. 7, where the outlet part of the vessel has been employed for finding the precision (-5.5 mm $< y < -1$ mm).

The fraction of bubbles estimated to fall outside the tube can then be translated into an estimate for the standard deviation as described in Section II-D. The fitted distribution for the bubble locations in the $y-z$ plane is shown in Fig. 8. For the $y-z$ plane 13% of the

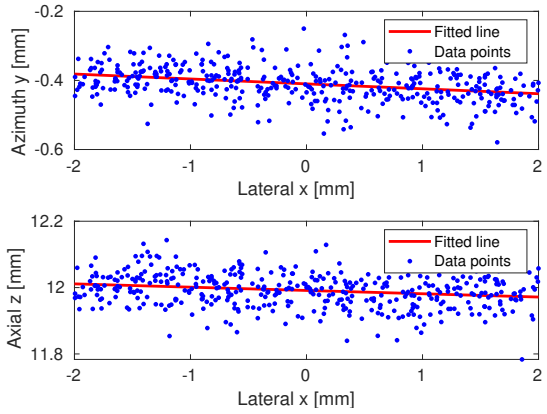

Fig. 6. Fitted line for calculating the center position of the vessel in the phantom in the $y-z$ plane.

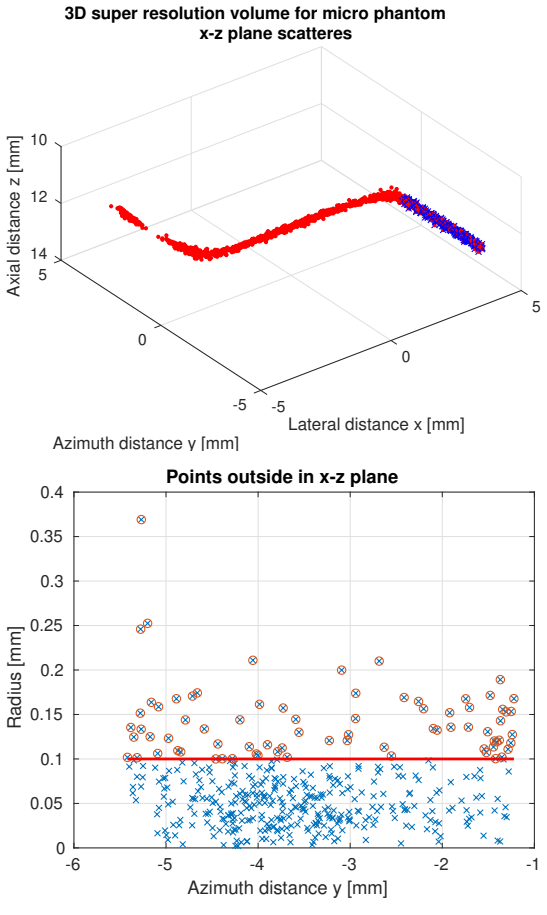

Fig. 7. Selected bubbles in the $x-z$ plane (blue dots) for estimating precision.

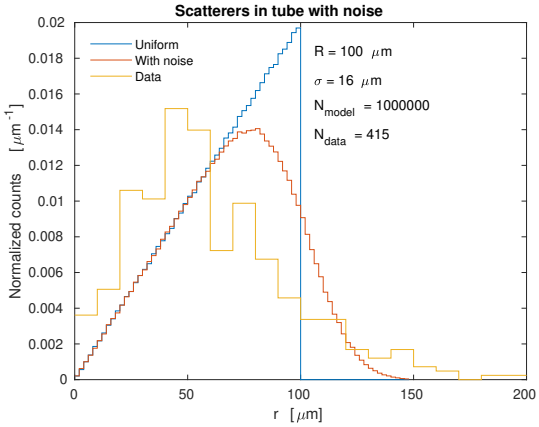

Fig. 8. Fitted distribution for the bubble locations in the $y-z$ plane.

bubbles fall outside the tube, which leads to a position uncertainty of 16.5 μm. Similarly, for the $x-z$ plane 18% of the bubbles are estimated to fall outside the tube, which leads to a position uncertainty of 23 μm.

IV. Discussion

A method for 3-D super resolution imaging has been developed based on a RC array and a pulse-inversion SA imaging sequence using 32 positive and negative emissions. A full volume is, thus, created in 64 emissions for a possible volume rate of 156 Hz at $f_{prf} = 10$ kHz, and the modest number of emissions makes it possible to have a 100 Hz volume rate down to a depth of 12 cm. The 3 MHz array's penetration depth is 14 cm due to its low frequency and fairly large size $(31\lambda \times 31\lambda)$. Only 62 elements were employed during receive, making it possible to implement the approach on a standard ultrasound console with the advantage that a limited amount of data is generated. A $\lambda/8$ sampling density on the receiving elements can be employed and will continuously generate 2.9 Gbytes/s, which is well within reach of modern ultrasound research scanners [11, 14, 28–30]. This is significantly less than for a fully populated array, where a 32×32 array yields 49 Gbytes/s for an array with one fourth the area of the RC probe used here.

The attained precision of the schemes was investigated using both a point micro-phantom and a flow micro-phantom with a 200 μm diameter tube. The point phantom yielded a localization precision of (20.7, 19.8, 9.1) μm in the x, y, z coordinates. The flow micro-phantom yielded an estimated radial precision of 16.5 μm in the $y-z$ plane, and 23 μm in the $x-z$ plane. Assuming the coordinate precisions are independent, the radial precision would be 15.4 μm in the $y-z$ plane, and 16.0 μm in the $x-z$ plane, when using the estimated precisions from the point phantoms. The $10.8 \times 10.8 \times 20$

μm^3 voxel size of the printer will give rise to tube-wall fluctuations, with an increase in precision, so the estimated precision for the two phantoms are therefore similar.

The precision should be compared to the emitted wavelength of 500 μm, and an improved localization of a factor of at least 20 times is attained in all three coordinates. The measured PSF has a size of $0.58 \times 1.05 \times 0.31$ mm^3 making it in theory possible to interrogate a volume 28,900 times smaller than a PSF limited system.

The main advantage of a 3-D system compared to the current 2-D systems is the increased resolution in the elevation plane. Current 2-D SR displays images averaged across the elevation plane thickness, which can often be 5-15 λ away from the elevation focus. The resolution is, thus, improved by a factor 100-300 times compared to a 1D probe, even though the number of elements is 3 times lower than a 192-elements 1D probe.

Several factors can be improved in the current setup and should be incorporated into a clinically useful 3-D SR imaging scheme. Currently, no motion correction is conducted, but the SA imaging scheme makes it possible to beamform a full volume at more than 100 Hz. This is sufficient to employ speckle tracking [31] in 3-D to yield and compensate for the motion as described for SA flow imaging [32, 33]. Although many schemes use very high frame rates with thousands images per second [6, 9] , it has been shown that a conventional linear array scan with frame rates at 54 Hz can yield excellent super resolution images with both motion estimation [34] and quantification of flow [35]. The 154 Hz volume rate should, thus, be sufficient for in-vivo imaging.

The fairly high velocity of 102.4 mm/s in the flow micro-phantom is used to prevent clogging of the phantom. This currently prevents the formation of tracks in the SR pipeline as is done for the PSF micro phantom, but further experiments should be conducted to lower the velocity, and maybe introduced a phantom with less sharp bends to prevent clogging. No efforts have been made to reduce false detections in the SR pipeline. Forming long tracks can significantly reduce the number of false detections, and this could potentially improve the precision of the location estimates.

The numbers of bubbles used here was sparse to make isolation easier. The acquisition length could be reduced, if more detections could be made per second. Methods for increasing the number of bubble detections have been the topic of a number of articles [36–38]. Such approaches can also be employed here, as full RF data are acquired and can be processed using more advanced schemes.

The RC array can also be improved. The current array is a 5-years old prototype PZT array with only 62 elements. The array has 8 non-functioning row elements and is slightly curved with a deviation around 0.1λ from a flat surface. This introduces phase errors and impedes image contrast. Other more advanced focusing schemes, like matched filter focusing, could also be used for increasing contrast [21, 39]. It is also possible to optimize the emission sequence for contrast agent enhancement, where amplitude modulation potentially could be used [40–42], and it could also be possible to optimize the imaging sequence with fewer emissions for yielding less data and higher volume rates [43]. Adding more elements to the probe can also increase resolution and thereby reduce acquisition time, as more bubbles can be separated. Early investigations have been made for a 192 + 192 RC array and showed an increased resolution proportional to the F-number and wavelength [44]. Such arrays can directly be used on modern ultrasound consoles with few modifications in the beamforming.

The approach can fairly easily be translated to clinical use by modifying our current 2-D super resolution pipeline to include searches and localizations in 3-D [34, 35]. The motion correction schemes developed for 2-D imaging and needed for in-vivo imaging can then also be applied [34]. The main clinical applications could be superficial structures, where the F-number in beamforming can be kept low. The penetration depth is 14 cm for this array and imaging scheme, which is beneficial for larger organs like the liver. The bubble density would have to be reduced for reliable detection, and the imaging region will only be within the rectilinear area of the probe. This can potentially be alleviated by using a lens in front of the array [45].

A first in-vivo target would be to scan a rat kidney as performed in [34, 35]. The acquisition time was between 1 and 10 minutes for a 2-D image, with 1 minute giving an overall rough view of the vasculature and 10 minutes giving precise quantitative data for the blood flow. We predict that the same scan times can be kept with the method presented here for a full volume, and maybe with a shorter time when employing more advanced SRI [36–38].

The high resolution will also give some future challenges. The RC array can image a volume of $31\lambda \times 31\lambda \times 280\lambda$, which, with a voxel size of $(10\mu\text{m})^3$, would yield 33 GVoxels. This might give some challenges in the display of such data.

V. Conclusion

A method for 3-D SRI has been investigated, where a 62+62 RC array was employed. A detection precision

better than 23 μm was attained in all three coordinates for both the SonoVue contrast agent flowing in a micro-phantom and the point micro-phantom. The precision was obtained using 1/8 of the elements employed in previous 3-D SRI, which reduces both the storage and processing demands by a factor of eight. The approach yielded an increase in volumetric resolution by a factor of more than 28,900 with a possible penetration depth down to 14 cm and corresponding increase in the amount of volumetric data to 10-40 GVoxels. Potentially a volume of $16 \times 16 \times 140$ mm^3 can be resolved with a voxel size of $(10\mu\text{m})^3$.

ACKNOWLEDGMENT

This work was financially supported by grant 82-2014-4 from the Danish National Advanced Technology Foundation, by grant 7050-00004B from Innovation Fund Denmark, and from BK Medical, Herlev, Denmark.

REFERENCES

[1] O. Couture, B. Besson, G. Montaldo, M. Fink, and M. Tanter, "Microbubble ultrasound super-localization imaging (MUSLI)," in *Proc. IEEE Ultrason. Symp.*, 2011, pp. 1285–1287.

[2] O. M. Viessmann, R. J. Eckersley, K. C. Jeffries, M. X. Tang, and C. Dunsby, "Acoustic super-resolution with ultrasound and microbubbles," *Phys. Med. Biol.*, vol. 58, pp. 6447–6458, 2013.

[3] M. Siepmann, G. Schmitz, J. Bzyl, M. Palmowski, and F. Kiessling, "Imaging tumor vascularity by tracing single microbubbles," *Proc. IEEE Ultrason. Symp.*, pp. 6 293 297, 1906–1908, 2011.

[4] M. A. O'Reilly and K. Hynynen, "A super-resolution ultrasound method for brain vascular mapping," *Med. Phys.*, vol. 40, no. 11, pp. 110 701–7, 2013.

[5] K. Christensen-Jeffries, R. J. Browning, M. Tang, C. Dunsby, and R. J. Eckersley, "In vivo acoustic super-resolution and super-resolved velocity mapping using microbubbles," *IEEE Trans. Med. Imag.*, vol. 34, no. 2, pp. 433–440, February 2015.

[6] C. Errico, J. Pierre, S. Pezet, Y. Desailly, Z. Lenkei, O. Couture, and M. Tanter, "Ultrafast ultrasound localization microscopy for deep super-resolution vascular imaging," *Nature*, vol. 527, pp. 499–502, November 2015.

[7] O. Couture, V. Hingot, B. Heiles, P. Muleki-Seya, and M. Tanter, "Ultrasound localization microscopy and super-resolution: A state of the art," *IEEE Trans. Ultrason., Ferroelec., Freq. Contr.*, vol. 65, no. 8, pp. 1304–1320, 2018.

[8] J. Zhu, E. M. Rowland, S. Harput, K. Riemer, C. H. Leow, B. Clark, K. Cox, A. Lim, K. Christensen-Jeffries, G. Zhang, J. Brown, C. Dunsby, R. J. Eckersley, P. D. Weinberg, and M.-X. Tang, "3D super-resolution US imaging of rabbit lymph node vasculature in vivo by using microbubbles," *Radiology*, vol. 291, no. 3, pp. 642–650, 2019.

[9] F. Lin, S. E. Shelton, D. Espindola, J. D. Rojas, G. Pinton, and P. A. Dayton, "3-D ultrasound localization microscopy for identifying microvascular morphology features of tumor angiogenesis at a resolution beyond the diffraction limit of conventional ultrasound," *Theranostics*, vol. 7, no. 1, pp. 196–204, 2017.

[10] K. Christensen-Jeffries, S. Harput, J. Brown, P. N. T. Wells, P. Aljabar, C. Dunsby, M. Tang, and R. J. Eckersley, "Microbubble axial localization errors in ultrasound super-resolution imaging," *IEEE Trans. Ultrason., Ferroelec., Freq. Contr.*, vol. 64, no. 11, pp. 1644–1654, 2017.

[11] J. A. Jensen, H. Holten-Lund, R. T. Nilsson, M. Hansen, U. D. Larsen, R. P. Domsten, B. G. Tomov, M. B. Stuart, S. I. Nikolov, M. J. Pihl, Y. Du, J. H. Rasmussen, and M. F. Rasmussen, "SARUS: A synthetic aperture real-time ultrasound system," *IEEE Trans. Ultrason., Ferroelec., Freq. Contr.*, vol. 60, no. 9, pp. 1838–1852, 2013.

[12] L. Petrusca, F. Varray, R. Souchon, A. Bernard, J. Y. Chapelon, H. Liebgott, W. A. N'Djin, and M. Viallon, "Fast volumetric ultrasound B-mode and Doppler imaging with a new high-channels density platform for advanced 4D cardiac imaging/therapy," *Applied Sciences (Switzerland)*, vol. 8, no. 2, pp. 200:1–15, 2018.

[13] S. Harput, K. Christensen-Jeffries, A. Ramalli, J. Brown, J. Zhu, G. Zhang, C. H. Leow, M. Toulemonde, E. Boni, P. Tortoli, R. J. Eckersley, C. Dunsby, and M. Tang, "3-D super-resolution ultrasound (SR-US) imaging with a 2-D sparse array," *arXiv preprint*, p. 1902.01608v1, 2019.

[14] E. Boni, L. Bassi, A. Dallai, F. Guidi, V. Meacci, A. Ramalli, S. Ricci, and P. Tortoli, "ULA-OP 256: A 256-channel open scanner for development and real-time implementation of new ultrasound methods," *IEEE Trans. Ultrason., Ferroelec., Freq. Contr.*, vol. 63, no. 10, pp. 1488–1495, 2016.

[15] C. E. Morton and G. R. Lockwood, "Theoretical assessment of a crossed electrode 2-D array for 3-D imaging," in *Proc. IEEE Ultrason. Symp.*, 2003, pp. 968–971.

[16] C. E. M. Démoré, A. Joyce, K. Wall, and G. Lockwood, "Real-time volume imaging using a crossed electrode array," *IEEE Trans. Ultrason., Ferroelec., Freq. Contr.*, vol. 56, no. 6, pp. 1252–1261, 2009.

[17] J. T. Yen, C. H. Seo, S. I. Awad, and J. S. Jeong, "A dual-layer transducer array for 3-D rectilinear imaging," *IEEE Trans. Ultrason., Ferroelec., Freq. Contr.*, vol. 56, no. 1, pp. 204–212, 2009.

[18] A. Sampaleanu, P. Zhang, A. Kshirsagar, W. Moussa, and R. Zemp, "Top-orthogonal-to-bottom-electrode (TOBE) CMUT arrays for 3-D ultrasound imaging." *IEEE Trans. Ultrason., Ferroelec., Freq. Contr.*, vol. 61, no. 2, pp. 266–276, 2014.

[19] M. F. Rasmussen, T. L. Christiansen, E. V. Thomsen, and J. A. Jensen, "3-D imaging using row–column-addressed arrays with integrated apodization — Part I: Apodization design and line element beamforming," *IEEE Trans. Ultrason., Ferroelec., Freq. Contr.*, vol. 62, no. 5, pp. 947–958, 2015.

[20] T. L. Christiansen, M. F. Rasmussen, J. P. Bagge, L. N. Moesner, J. A. Jensen, and E. V. Thomsen, "3-D imaging using row–column-addressed arrays with integrated apodization — part II: Transducer fabrication and experimental results," *IEEE Trans. Ultrason., Ferroelec., Freq. Contr.*, vol. 62, no. 5, pp. 959–971, 2015.

[21] H. Bouzari, M. Engholm, S. I. Nikolov, M. B. Stuart, E. V. Thomsen, and J. A. Jensen, "Imaging performance for two row-column arrays," *IEEE Trans. Ultrason., Ferroelec., Freq. Contr.*, vol. 66, no. 7, pp. 1209–1221, 2019.

[22] M. Engholm, H. Bouzari, T. L. Christiansen, C. Beers, J. P. Bagge, L. N. Moesner, S. E. Diederichsen, M. B. Stuart, J. A. Jensen, and E. V. Thomsen, "Probe development of CMUT and PZT row–column-addressed 2-D arrays," *Sens. Actuators A: Phys.*, vol. 273, pp. 121–133, 2018.

[23] M. B. Stuart, M. Schou, and J. A. Jensen, "Row-column beamforming with dynamic apodizations on a GPU," in *Proc. SPIE Med. Imag.*, 2019, pp. 1–7, paper number 10955-20.

[24] J. A. Jensen and N. B. Svendsen, "Calculation of pressure fields from arbitrarily shaped, apodized, and excited ultrasound transducers," *IEEE Trans. Ultrason., Ferroelec., Freq. Contr.*, vol. 39, no. 2, pp. 262–267, 1992.

[25] J. A. Jensen, "Field: A program for simulating ultrasound systems," *Med. Biol. Eng. Comp.*, vol. 10th Nordic-Baltic Conference on Biomedical Imaging, Vol. 4, Supplement 1, Part 1, pp. 351–353, 1996.
[26] ——, "A multi-threaded version of Field II," in *Proc. IEEE Ultrason. Symp.* IEEE, 2014, pp. 2229–2232.
[27] M. L. Ommen, M. Schou, R. Zhang, C. A. V. Hoyos, J. A. Jensen, N. B. Larsen, and E. V. Thomsen, "3D printed flow phantoms with fiducial markers for super-resolution ultrasound imaging," in *Proc. IEEE Ultrason. Symp.*, 2018, pp. 1–4.
[28] J. A. Jensen, O. Holm, L. J. Jensen, H. Bendsen, S. I. Nikolov, B. G. Tomov, P. Munk, M. Hansen, K. Salomonsen, J. Hansen, K. Gormsen, H. M. Pedersen, and K. L. Gammelmark, "Ultrasound research scanner for real-time synthetic aperture image acquisition," *IEEE Trans. Ultrason., Ferroelec., Freq. Contr.*, vol. 52, no. 5, pp. 881–891, May 2005.
[29] P. Tortoli and J. A. Jensen, "Introduction to the special issue on novel equipment for ultrasound research," *IEEE Trans. Ultrason., Ferroelec., Freq. Contr.*, vol. 53, no. 10, pp. 1705–1706, Oct. 2006.
[30] E. Boni, A. C. H. Yu, S. Freear, J. A. Jensen, and P. Tortoli, "Ultrasound open platforms for next-generation imaging technique development," *IEEE Trans. Ultrason., Ferroelec., Freq. Contr.*, vol. 65, no. 7, pp. 1078–1092, 2018.
[31] G. E. Trahey, J. W. Allison, and O. T. von Ramm, "Angle independent ultrasonic detection of blood flow," *IEEE Trans. Biomed. Eng.*, vol. BME-34, no. 12, pp. 965–967, 1987.
[32] S. I. Nikolov and J. A. Jensen, "In-vivo synthetic aperture flow imaging in medical ultrasound," *IEEE Trans. Ultrason., Ferroelec., Freq. Contr.*, vol. 50, no. 7, pp. 848–856, 2003.
[33] K. L. Gammelmark and J. A. Jensen, "2-D tissue motion compensation of synthetic transmit aperture images," *IEEE Trans. Ultrason., Ferroelec., Freq. Contr.*, vol. 61, no. 4, pp. 594–610, April 2014.
[34] J. A. Jensen, S. I. Nikolov, K. L. Hansen, M. B. Stuart, C. A. V. Hoyos, M. Schou, M. L. Ommen, S. H. Øygard, L. T. Jørgensen, M. S. Traberg, T.-Q. Nguyen, E. V. Thomsen, N. B.Larsen, C. Beers, and et al., "History and latest advances in flow estimation technology: From 1-D in 2-D to 3-D in 4-D," in *Proc. IEEE Ultrason. Symp.*, 2019, pp. 1–4.
[35] S. B. Andersen, C. A. V. Hoyos, I. Taghavi, F. Gran, K. L. Hansen, C. M. Sørensen, and J. A. J. M. B. Nielsen, "Super-resolution ultrasound imaging of rat kidneys before and after ischemia-reperfusion," in *Proc. IEEE Ultrason. Symp.*, 2019, pp. 1–4.
[36] E. Kanoulas, M. Butler, C. Rowley, V. Voulgaridou, K. Diamantis, W. C. Duncan, A. Mcneilly, M. Averkiou, H. Wijkstra, M. Mischi, R. S. Wilson, W. Lu, and V. Sboros, "Super-resolution contrast-enhanced ultrasound methodology for the identification of in vivo vascular dynamics in 2d," *Investigative Radiology*, vol. 54, no. 8, pp. 500–516, 2019.
[37] A. Bar-Zion, O. Solomon, C. Tremblay-Darveau, D. Adam, and Y. C. Eldar, "Sushi: Sparsity-based ultrasound super-resolution hemodynamic imaging," *IEEE Trans. Ultrason., Ferroelec., Freq. Contr.*, vol. 65, no. 12, pp. 2365–2380, 2018.
[38] O. Solomon, R. J. van Sloun, H. Wijkstra, M. Mischi, and Y. C. Eldar, "Exploiting flow dynamics for super-resolution in contrast-enhanced ultrasound," *IEEE Trans. Ultrason., Ferroelec., Freq. Contr.*, p. Early Access, 2019.
[39] J. T. Yen, "Beamforming of sound from two-dimensional arrays using spatial matched filters," *J. Acoust. Soc. Am.*, vol. 134, no. 5, pp. 3697–3704, 2013.
[40] V. Mor-Avi, E. G. Caiani, K. A. Collins, C. E. Korcarz, J. E. Bednarz, and R. M. Lang, "Combined assessment of myocardial perfusion and regional left ventricular function by analysis of contrast-enhanced power modulation images," *Circulation*, vol. 104, no. 3, pp. 352–357, 2001.
[41] R. J. Eckersley, C. T. Chin, and P. N. Burns, "Optimising phase and amplitude modulation schemes for imaging microbubble contrast agents at low acoustic power," *Ultrasound Med. Biol.*, vol. 31, no. 2, pp. 213–219, 2005.
[42] C. Tremblay-Darveau, R. Williams, L. Milot, M. Bruce, and P. N. Burns, "Visualizing the tumor microvasculature with a nonlinear plane-wave Doppler imaging scheme based on amplitude modulation," *IEEE Trans. Med. Imag.*, vol. 35, no. 2, pp. 699–709, 2016.
[43] R. Moshavegh, J. Jensen, C. A. Villagomez-Hoyos, M. B. Stuart, M. C. Hemmsen, and J. A. Jensen, "Optimization of synthetic aperture image quality," in *Proc. SPIE Med. Imag.*, vol. 9790, 2016, pp. 97 900Z–97 900Z–9.
[44] M. Schou, A. S. Havreland, M. Engholm, M. B. Stuart, E. V. Thomsen, and J. A. Jensen, "Design of a novel zig-zag 192+192 row column addressed transducer: A simulation study," in *Proc. IEEE Ultrason. Symp.*, 2018, pp. 1–4.
[45] H. Bouzari, M. Engholm, C. Beers, S. I. Nikolov, M. B. Stuart, E. V. Thomsen, and J. A. Jensen, "Curvilinear 3-D imaging using row–column addressed 2-D arrays with a diverging lens: Phantom study," *IEEE Trans. Ultrason., Ferroelec., Freq. Contr.*, vol. 65, no. 7, pp. 1182–1192, 2018.

Jørgen Arendt Jensen (M'93-SM'02-F'12) received the MSc degree in 1985, the Ph.D. degree in 1989, and the Dr.Techn. degree all from the university in 1996. Since 1993, he has been a Full Professor of Biomedical Signal Processing with the Department of Health Technology, Technical University of Denmark. He has been the founder and head of the Center for Fast Ultrasound Imaging since its inauguration in 1998. CFU has contributed with innovations in transverse oscillation vector flow imaging, synthetic aperture flow imaging in 2-D and 3-D, ultrasound simulation, research scanners, and row-column probes and beamforming. He has published more than 500 journal and conference papers on signal processing and medical ultrasound and the book Estimation of Blood Velocities Using Ultrasound (Cambridge Univ. Press), 1996. He is also the developer and maintainer of the Field II simulation program. He has been a visiting scientist at Duke University, Stanford University, and the University of Illinois at Urbana-Champaign. He was founder and head of the Biomedical Engineering group from 2007 to 2010. In 2003, he was one of the founders of the biomedical engineering program in Medicine and Technology, which is a joint degree program between the Technical University of Denmark and the Faculty of Health and Medical Sciences at the University of Copenhagen. The degree is one of the most sought-after engineering degrees in Denmark. He was chairman of the study board from 2003 to 2010 and Adjunct Professor with the University of Copenhagen from 2005 to 2010. He has given a number of short courses on simulation, synthetic aperture imaging, and flow estimation at international scientific conferences and teaches biomedical signal processing and

medical imaging at the Technical University of Denmark. His research is centered around simulation of ultrasound imaging, synthetic aperture imaging, vector blood flow estimation, 3-D and super resolution imaging, row-column probes, and construction of ultrasound research systems. He has educated 41 PhD students and currently advises 17 PhD students. Dr. Jensen has given more than 60 invited talks at international meetings and received several awards for his research, most recently the Grand Solutions Prize from the Danish Minister of Science, the order of the Dannebrog by her Majesty the Queen of Denmark, and the Rayleigh award from the UFFC Society in the field of Ultrasonics in 2019.

Martin Lind Ommen received the M.Sc. degree in Physics and Nanotechnology from the Technical University of Denmark, Lyngby, Denmark, in 2017. He is currently a Ph.D. student with the Biomedical Engineering Section, Department of Health Technology at the Technical University of Denmark. His current research interests include micro- and nanofabrication in general, in particular the fabrication of capacitive micromachined ultrasonic transducers (CMUTs), as well as phantom fabrication, with a current focus on stereolithographic fabrication of micro-flow- and scatter-phantoms.

Sigrid Husebø Øygard is a PhD candidate at DTU Health Tech in the Center for Fast Ultrasound Imaging. Sigrid recieved her BEng in Acoustical Engineering from the Institute of Sound and Vibration at the University of Southampton in 2016, where she specialized in bubble acoustics. She recieved her MSc in Physics with a focus on theoretical acoustics from the University of Bergen in 2018. Her research interests include 3D ultrasound imaging, super resolution imaging, and bubble acoustics.

Mikkel Schou was born in 1990. He received the M.Sc. degree in biomedical engineering from the Technical University of Denmark, Kongens Lyngby, Denmark, and the University of Copenhagen, Copenhagen, Denmark, in 2017. He is currently pursuing the Ph.D. degree in biomedical engineering with the Center for Fast Ultrasound Imaging, Technical University of Denmark. The topic of his Ph.D. research is 3-D ultrasound Perfusion and Flow imaging using Row-Column Arrays.

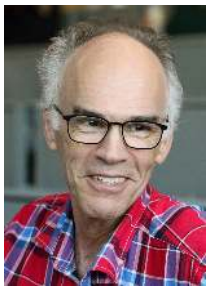

Thomas Sams received his MSc in Physics at the Niels Bohr Institute, University of Copenhagen (1986), where he also did his PhD on collective vibrations in nuclei (1991). He has worked for a 10 years on patterns in natural backgrounds at the Danish Defence Research Est. Since 2005 he has been an Associate Professor in Biomedical Engineering at the Technical University of Denmark, where he heads a research group in Cellular Signaling and Bioransport and the Biomedical Engineering Section. The common theme in his research is on the understanding of collective behavior in systems composed of smaller building blocks, including bacterial cell communities, patterns in yeast, patterns in sand ripples, and neural networks. He has worked as a post-doc at Saclay, France, the Niels Bohr Institute, and as a visiting researcher in Los Alamos, USA, and at the University of Cambridge, UK.

Mathias Bo Stuart received the M.Sc. and Ph.D. degrees in Computer Engineering from the Technical University of Denmark, Lyngby, Denmark in 2006 and 2010 respectively. He is currently an Associate Professor with the Biomedical Engineering Section, Department of Health Technology at the Technical University of Denmark. His research interests include synthetic aperture methods for both anatomical and flow imaging in both 2-D and 3-D, ultrasound systems, and real-time implementations of ultrasound processing algorithms.

Christopher Beers received the M.S. degree in acoustics from Pennsylvania State University, State College, PA, USA, in 2007, where his thesis research explored end-element anomalies in medical ultrasound transducer arrays. He has been with BK Medical, State College, PA, USA, since 2007 (formerly Sound Technology), where he develops transducer technology and designs commercial medical ultrasound probes.

Erik Vilain Thomsen was born in Aarhus, Denmark, in 1964. He received the M.Sc. degree in physics from the University of Southern Denmark, Odense, Denmark, in 1992 and the Ph.D. degree in electrical engineering from the Technical University of Denmark (DTU), Kongens Lyngby, Denmark, in 1998. He is currently Professor at the Department of Health Technology, Technical University of Denmark (DTU) where he is also the Head of the MEMS Applied Sensors Group and Head of Division with responsibility for the educations in healthcare engineering. He teaches classes in solid state electronics, microtechnology, and nano and microfabrication. His current research interests include all aspects of capacitive micromachined ultrasonic transducers (CMUTs), general MEMS technology, and piezoelectric MEMS. Dr. Thomsen received the Danish National Advanced Technology Foundation Grand Solution Prize in 2017, the AEG Electron Prize in 1995, and has received several teaching awards at DTU.

Niels Bent Larsen received his MSc and PhD degrees in chemistry in 1993 and 1997, both from University of Copenhagen. He is currently Professor and Section Head at the Department of Health Technology. His current research interests are in high-resolution 3D printing of compliant hydrogel materials to recreate the vascular network of body organs to enable advanced in vitro organ models.

Borislav Gueorguiev Tomov received a M. Sc. degree in Electronics Engineering from the Technical University of Sofia, Bulgaria, in 1996, and a Ph.D. degree in Medical Electronics from the Technical University of Denmark in 2003. He is currently Senior Researcher at the Center for Fast Ultrasound imaging, Department of Health Technology, Technical University of Denmark. His research interests include medical ultrasound signal processing, and ultrasound scanner architectures and implementations.